PAPER

Investigating thermal conductivity and mechanical properties of a hybrid material based on cellulose nanofibers and boron nitride nanotubes using molecular dynamics simulations

To cite this article: Upamanyu Ray *et al* 2024 *J. Phys. D: Appl. Phys.* **57** 185302

IOP Publishing Journal of Physics D: Applied Physics
J. Phys. D: Appl. Phys. **57** (2024) 185302 (9pp) https://doi.org/10.1088/1361-6463/ad2335

Investigating thermal conductivity and mechanical properties of a hybrid material based on cellulose nanofibers and boron nitride nanotubes using molecular dynamics simulations

Upamanyu Ray[1], **Zhenqian Pang**[2,3,*] **and Teng Li**[1,*]

[1] Department of Mechanical Engineering, University of Maryland, College Park, MD 20742, United States of America
[2] Department of Architecture, College of Civil Engineering and Architecture, Zhejiang University, Hangzhou 310027, People's Republic of China
[3] Smart Materials for Architecture Research Lab, Innovation Center of Yangtze River Delta, Zhejiang University, Jiaxing 314100, People's Republic of China

E-mail: zqpang@zju.edu.cn and lit@umd.edu

Received 23 October 2023, revised 2 January 2024
Accepted for publication 26 January 2024
Published 8 February 2024

Abstract

Cellulose nanofibers (NFCs) have emerged as a preferred choice for fabricating nanomaterials with exceptional mechanical properties. At the same time, boron nitride nanotubes (BNNTs) have long been favored in thermal management devices due to their superior thermal conductivity (k). This study uses reverse non-equilibrium molecular dynamics (MD) simulations to investigate k for a hybrid material based on NFCs and BNNTs. The result is then compared with pure NFC and BNNT-based structures with equivalent total weight content to elucidate how incorporating BNNT fillers enhances k for the hybrid system. Furthermore, the fundamental phonon vibration modes responsible for driving thermal transport in NFC-based materials upon incorporating BNNTS are identified by computing the vibrational density of states from the Fourier transform analysis of the averaged mass-weighted velocity autocorrelation function. Additionally, MD simulations demonstrate how both NFCs and BNNTs synergistically improve the constituting hybrid structure's mechanical properties (e.g. tensile strength and stiffness). The overarching aim is to contribute towards the engineered design of novel functional materials based on nanocellulose that simultaneously improve crucial physical properties pertaining to thermal transport and mechanics.

Keywords: nanocellulose, boron nitride nanotube, molecular dynamics, thermal conductivity, strength, stiffness

* Authors to whom any correspondence should be addressed.

1. Introduction

Cellulose, the widely available renewable bio-polymer, has recently emerged as a promising candidate in sustainable materials design [1–6]. Nanomaterials based on cellulose nanofibers (NFCs) display an anomalous scaling law of simultaneous increase in strength and toughness [7], two mechanical properties that conventionally conflict with each other. These superior mechanical properties in NFC-based nanomaterials stem from their unique morphology that can offer numerous bonding sites (hydrogen bonding and other noncovalent interactions) for functionalization [8, 9]. However, the thermal conductivity (k) of NFCs [10, 11] is relatively low ($\sim$1.45 W mK^{-1}), although it still surpasses that of conventional polymers by approximately six times [12]. Enhancing the thermal conductivity of NFC-based materials [13–15] through noncovalent functionalization may open opportunities to develop composites with appealing thermo-mechanical properties.

On the contrary, single-walled boron nitride nanotubes (BNNTs) [16–18] hold great potential as fillers for developing advanced thermal management materials due to their high thermal conductivity ($\sim$400 W mK^{-1}) and thermal stability up to temperatures around 800 °C. However, reproducing the remarkable properties of BNNT to bulk is the primary challenge. Recent advancements have overcome initial obstacles in fabricating pure BNNT films through novel methods such as gram-scale fabrication promoters [19] and scalable techniques involving dissolving BNNTs in acids [20]. Nevertheless, the bulk form of BNNT films still exhibits relatively low values of k at 18 W mK^{-1} [21]. Furthermore, hybridizing BNNTs with polymers to fabricate composites continues to yield values of k less than 5 W mK^{-1} [22, 23], which might be insufficient for applications requiring high thermal conductivity.

The primary challenge to achieving high thermal conductivity in BNNT filler-based polymer composites is overcoming the interfacial thermal resistance between adjacent BNNTs, which may lead to aggregate formation. Research has addressed this issue by functionalizing BNNTs with polymers such as PVA [24, 25], ether imides [26], and epoxy resins [27]. To this end, NFCs have emerged as a potential bio-polymer to effectuate non-covalent hybridization with BNNT fillers and enhance the thermal conductivity of the resulting material. For instance, in NFC/BNNT-based materials, k increased significantly to approximately 20.9 W mK^{-1}, representing an improvement of around 14.3 times compared to conventional polymers [28]. In a separate study, a BNNT/NFC-based nanocomposite demonstrated a high value of k ($\sim$21.39 W mK^{-1}) [12] due to reduced interfacial resistance facilitated by the strong interactions between NFCs and BNNTs. However, no systematic study currently explains why incorporating BNNTs into NFC-based materials increases k; this gap may be attributed to the difficulty in conducting characterization experiments at length scales below 10^{-10} m. A modeling-driven research approach could bridge this gap and is the focus of our present investigation.

This study employs molecular dynamics (MD) simulations to investigate the thermal conductivity enhancement in nanocellulose-based materials due to incorporating BNNTs. The reverse non-equilibrium MD (RNEMD) technique is utilized to compute k. At the same time, the vibrational density of states (DOS) analysis helps identify the phonon modes responsible for efficient heat transfer. Furthermore, the synergistic combination of NFCs and BNNTs, increasing the mechanical properties in derived hybrid structures, is explored. This modeling-based approach inspires sustainable materials design for NFC/BNNT composites with exceptional mechano-thermal properties.

2. MD modeling methodology

The reported MD simulations have been carried out using the parallelized, open-source package LAMMPS [29, 30]. ReaxFF [31, 32] force field that can capture the atomic interactions of complex reactions through bond-order details has been found suitable for boron–nitride/cellulose-based systems [33] and applied in this study. The time step for all the simulations is 0.5 fs. Periodic boundary conditions are imposed in all directions, an example of which has been depicted by the red box in figure 2(a). To elucidate the length effect clearly, the BNNT has been truncated and then both ends of each nanotube have been passivated with the −H atoms (as shown in the atomic structure within the red box of figure 2(a)). Sufficient vacuum space has been incorporated between the ends of BNNT and the boundaries of the simulation box to prevent the overlap with their own periodic images. Model equilibration is performed to achieve a global temperature of $\sim$300 K and pressure of $\sim$1 atm using Nose–Hoover isothermal–isobaric, canonical, and microcanonical ensembles for a total time of 3.5 ns, in the absence of any external constraints.

The thermal conductivity is computed using the RNEMD method proposed by Müller–Plathe [34]. The equilibrated model is numerically divided into spatial bins along their length L, which is also the heat transport direction (z-axis). Kinetic energies are swapped every 150 fs between the 'hot' (middle) bin and the 'cold' (two ends) bins, because of which a temperature gradient is imposed on the model along the axis. This process continued for a total duration of 5 ns. The temperature variation was monitored during the last 2 ns within this timeframe. To ensure that the system reached a steady state, the temperature was closely observed and found to remain reasonably constant with minor fluctuations of $\pm$2.5 K when maintaining a global system temperature of 300 K. The energy exchanges were continued for an additional 2 ns performing time averages every 50 fs to assess the total energy transferred and the temperature gradient. The final k is computed using equation (1) as described in [34]:

$$k = \frac{m\sum v_1^2 - v_2^2}{2t\,A\,\frac{\mathrm{d}T}{\mathrm{d}z}} \tag{1}$$

where the numerator outputs the total kinetic energy exchanges through the simulated structure, t is the total time spent in the energy exchanges, A is the cross-sectional area and $\frac{dT}{dz}$ is the average temperature gradient obtained from the simulations. The cross-sectional area (xy) of the simulation box perpendicular to the heat transfer direction is used to determine A. The temperature gradient ($\frac{dT}{dz}$) along the thermal transport (z) direction is obtained from the arithmetic mean of the two linear regimes in every inverted 'V' shaped temperature profile of a simulated model.

To calculate the vibrational DOS, the simulations are performed after equilibration for an additional 1 ns under the canonical ensemble at 300 K, with atomic trajectories every 50 ps. An additional 5 ps then extend each sampled trajectory, and the atomic velocities are recorded every 0.001 ps. The data is utilized to compute the time-translation invariance of the mass-weighted velocity autocorrelation function (VACF). The correlation time is set as 4.5 ps. A Fourier-transformed of the overall average VACFs yields the DOS spectra, as described by the following equation (2) below:

$$P\ (\omega) = \frac{1}{\sqrt{2\pi}} \int_0^{\infty} e^{i\omega t} \left[\sum_{j=1}^{N} m_j v_j\,(t)\,.\,m_j v_j\,(0) \right] \mathrm{d}\omega \qquad (2)$$

where the frequency of vibration is represented by ω, and the mass and velocities of atom j are represented by m_j and v_j, respectively. The resolution of the obtained DOS spectra is 0.061 THz.

The mechanistic study results are obtained by deforming the equilibrated simulation box at a tensile engineering strain rate of 10^{10} s^{-1}. In the engineering stress–strain plots that are shown, the reported stress is the normal stress component on the simulation box along the tensile loading direction. The entire deformation simulation was carried out for 50 ps with time averages of the engineering stress-strain values performed every 1.0 ps.

3. Results and discussion

To investigate the effect of increasing length (L) of a single NFC molecular chain (figure 1(a)) on k, six models of single-chain NFC molecules are constructed with values of $L = 10$ nm, 20 nm, 30 nm, 35 nm, 40 nm, and 50 nm. A representative temperature profile for the model with $L = 20$ nm, obtained by employing RNEMD calculations, is shown in figure 1(b). The cross-sectional area (A) used to compute k is determined as 0.33 nm^2, which closely matches previous results [14] (0.32 nm^2) obtained from non-equilibrium MD simulations for a single NFC chain, thus validating the adopted method and force-field. Additionally, the calculated values of k for all NFC molecules are between 0.8–1.69 W mK^{-1}, which aligns with experimental studies measuring in-plane thermal conductivity of nanocellulose (0.6–2.5 W mK^{-1} [35]). On observing the trend of thermal conductivity change for the six models (figure 1(c)), it is observed that k values increase with an increase in length. The enhancement of k with increased L can be attributed to the phonon scattering. Phonons, which are discrete lattice vibrational elastic waves, serve as major carriers of thermal transport in nanostructures. With increased chain length, phonon transport and scattering increase, raising its mean free path and increasing k. The rate of increase tends to decrease after reaching a certain length (∼35 nm). To further explore this phenomenon, the vibrational DOS (figures 1(d)–(f)) is calculated for two NFC chains having $L = 10$ nm (black lines) and 40 nm (red lines). Figures 1(d)–(f) denote the total phonon DOS along in-plane heat transport direction ($-z$), out-of-plane $-x$, and out-of-plane $-y$ directions, respectively. First and foremost, all the plots in each direction follow a similar pattern, indicating similar phonon properties for different lengths of the NFC molecular chains. In a spectrum, low-frequency waves have a higher wave number and, thus, a more extended range. So, low-frequency peaks (here, ∼0–20 THz) are monitored as they represent the dominant vibrational models that cause the thermal conductivity change. The low-frequency peaks of the vibrational spectra distributed across 0 THz–20 THz for NFC molecules have been observed in previous literature [14]. Here, it is observed that the first prominent peak in the low frequency of spectra along the heat transport ($-z$) direction occurs at approximately 5.49 THz (inset, figure 1(d)) and 6.04 THz (inset, figure 1(d)) for NFCs with $L = 10$ nm and $L = 40$ nm, respectively. This spectral shift towards higher frequency indicates an increase in the energy-carrying capacity of the phonons as NFC molecule lengths increase, resulting in an enhanced k. Similarly, although less conspicuous, a shift in frequency from low to high with increasing lengths of NFCs is also observed consistently for $-x$ and $-y$ directions that are perpendicular to thermal transport (figures 1(e) and (f)).

In addition to individual NFC molecular chains, the variation of k in single-walled BNNTs with increasing nanotube length (L) (figure 2(a)) is also investigated. Different values of $L = 10$ nm, 20 nm, 30 nm, 40 nm, 50 nm, and 60 nm are chosen. In addition, a previous study by Huang *et al* [18] observes that for 20 nm long BNNTs with varying chirality, the thermal conductivity (k) values at 300 K range from 80 W mK^{-1} to 90 W mK^{-1}. The slight fluctuations in k were attributed to minor changes in lattice vibrational modes. Hence, different chirality among BNNTs did not significantly impact the overall thermal conductivity. Given that this study aims to investigate the influence of incorporating BNNTs on k for NFC-based materials, all models utilized BNNTs with a constant chirality of (10, 10). The temperature profile obtained from RNEMD simulation of BNNT having $L = 20$ nm is shown in figure 2(b). The thermal conductivity (k) of BNNTs increases with an increase in their length (L), as shown in figure 2(c). However, beyond a certain length (approximately $L \sim 35$ nm in this study), the rate of increase of k starts to diminish. From figure 2(c), it can be observed that the increment in k for BNNTs with $L = 35$ nm, $L = 40$ nm, and $L = 50$ nm is relatively smaller compared to the shorter lengths, and the data points for k are higher with increasing

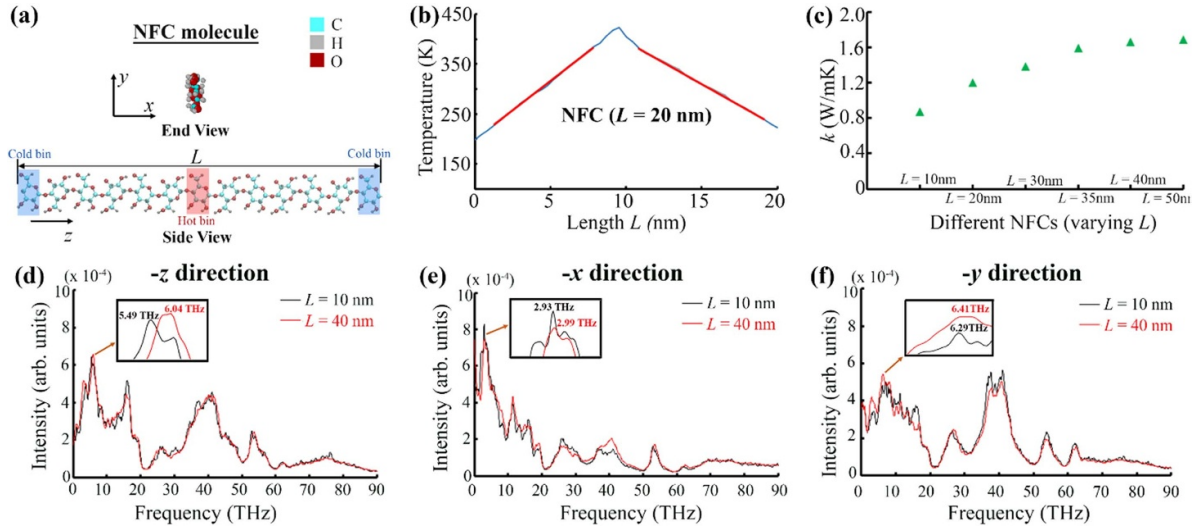

Figure 1. (a) Initial model of a cellulose (NFC) molecular chain of length L; (b) Temperature profile (K) of an NFC molecular chain along the thermal transport direction. For this profile, $L = 20$ nm (c) Variation of k (W mK^{-1}) with increasing lengths ($L = 10$ nm, 20 nm, 30 nm, 35 nm, 40 nm, 50 nm) of NFC molecular chain models; (d-f) Comparison of vibrational density of states (DOS) for two NFC molecular chain models with $L = 10$ nm (black) and 40 nm (red), along the (d) $-z$ direction, and the out-of-plane (e) $-x$ and (f) $-y$ directions.

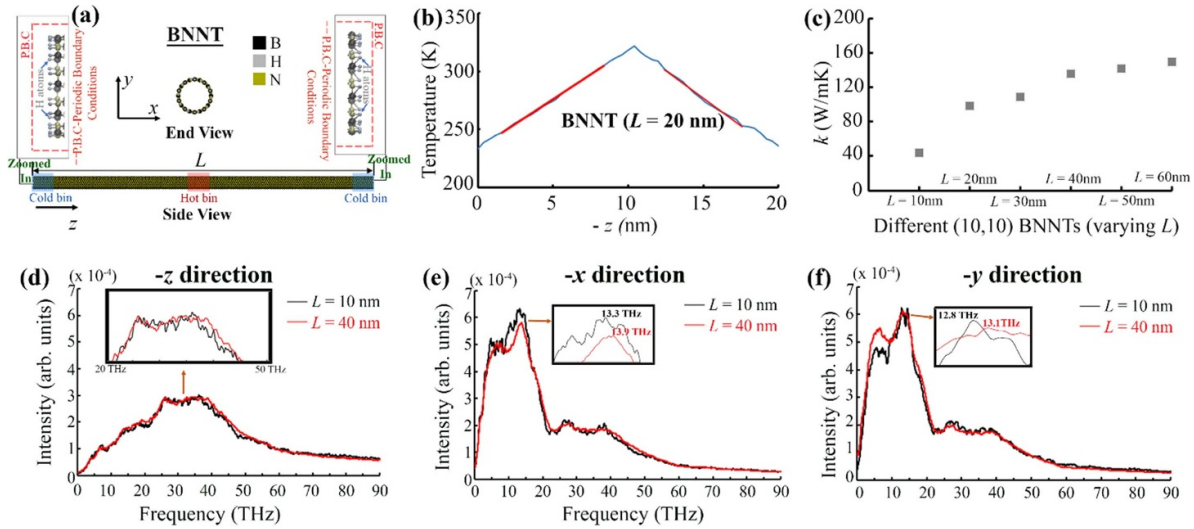

Figure 2. (a) Initial snapshot of a (10,10) BNNT model having length L. (b) Temperature profile (K) of the BNNT having $L = 20$ nm along $-z$, the heat transport direction. (c) Variation of k (W mK^{-1}) in BNNT models having different L; (d)–(f) Comparison of vibrational density of states (DOS) in two BNNT models having lengths $L = 10$ nm (black) and 40 nm (red)} along the (d) heat transport ($-z$) direction, and the out-of-plane (e) $-x$ and (f) $-y$ directions.

L, but closer to being equal. Furthermore, for a BNNT with $L = 20$ nm, the calculated k value is found to be approximately equal to 98.47 W mK^{-1}, which reasonably matches well with the range of 110–130 W mK^{-1} predicted by previous MD simulations [18] for a BNNT (10, 10) at 300 K. To identify the vibrational modes influencing thermal transport in BNNTs, total phonon DOS spectra along three perpendicular directions are compared for two BNNTs with $L = 10$ nm (black lines in figures 2(d)–(f)) and $L = 40$ nm (red lines in figures 2(d)–(f)). The DOS spectra of these nanotubes along thermal transport (-z) direction and out-of-plane transverse directions ($-x$ and $-y$) are shown in figures 2(d)–(f), respectively. Each spectrum along a specific direction ($-z$ or $-x$ or $-y$) exhibits a reasonably comparable shape for BNNTs with increasing lengths. This indicates similar phonon properties along directions having similar morphology. It is also to be noted that for BNNTs, the phonon spectra along $-x$ and $-y$ directions are also closely similar to each other, an observation absent for NFCs discussed in figure 1. This might be attributed to the fact that the BNNTs have a similar atomic distribution in both $-x$ and $-y$ directions across the circular cross-section ($-xy$ plane) of the nanotube. However, the perpendicular axes across the cross-sectional directions ($-x$ and $-y$ as shown in figure 1(a)) in NFCs are dissimilar. Therefore,

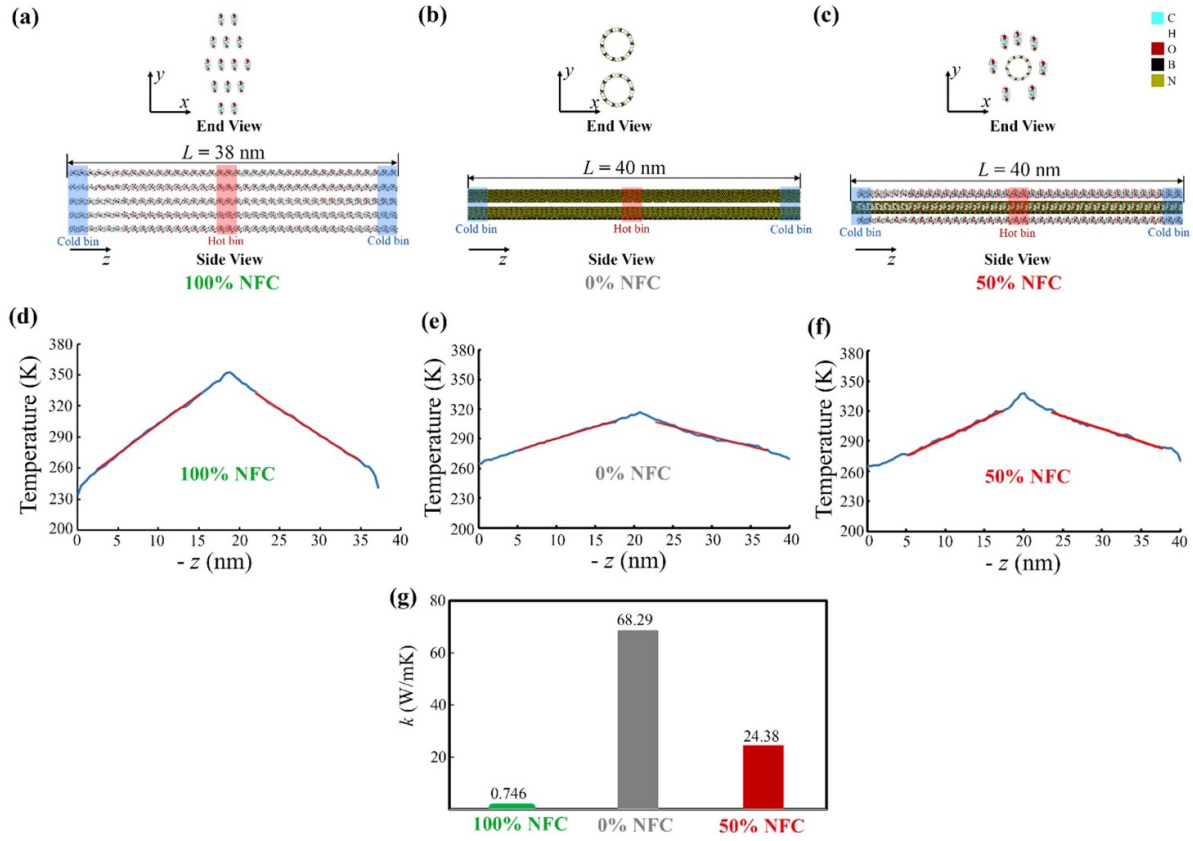

Figure 3. Comparison of k (W mK^{-1}) in three different models ('100% NFC', '0% NFC' and hybrid ('50% NFC')) having similar weight content; (a) initial snapshot of a pure cellulose model ('100% NFC') used to compute k by plotting the (d) temperature profile (K) along the thermal transport ($-z$) direction; (b) snapshot of a pure BNNT model ('0% NFC') used to compute k by plotting the (e) temperature profile (K) along the heat transfer ($-z$) direction; (c) initial snapshot of a hybrid NFC-BNNT model with ∼50% weight content of BNNTs ('50% NFC') and (f) its temperature distribution (K) along the thermal transport ($-z$) direction; (g) comparison of k elucidating the effect of BNNT addition on thermal transport of hybrid.

atom vibrations and discrete lattice waves (phonons) resulting from cross-sectional radial modes of BNNTs, are comparable. For the BNNTs, the in-plane vibrational modes along the heat transfer ($-z$) direction are distributed across at a relatively high frequency in the range of 26.4 THz–37.1 THz (figure 2(d)) and thus are not dominant modes in the thermal transport. The in-plane modes also do not show any conspicuous spectral shift towards high frequency when L increases from 10 nm to 40 nm. The dominant, low-frequency peaks representing the out-of-plane transverse vibrational modes are illustrated by black (for BNNT with L = 10 nm) and red (for BNNT with L = 40 nm) fonts in figures 2(e) and (f). For the BNNT with L = 10 nm, low-frequency peaks are at 13.3 THz along -x (figure 2(e)) and 12.8 THz (figure 2(f)) along $-y$ directions. The corresponding peaks for the BNNT with L = 40 nm are 13.9 THz along $-x$ and 13.1 THz along $-y$. The corresponding peaks for the BNNT with L = 40 nm are increased to 13.9 THz along $-x$ and 13.1 THz along $-y$. Considering the radial symmetry, it can be inferred that the dominant influence on the thermal transport of BNNTs is attributed to the radial ($-x$ and $-y$) vibrational modes, namely out-of-plane modes, rather than the in-plane modes along $-z$. Shifting to a higher frequency in the vibrational spectra implies increased phonon energy-carrying capacity. This indicates greater phonon-phonon scattering, amplifying the k value as the L in BNNTs increases.

After evaluating k in pure NFC molecule and pure BNNT, the study is extended to a hybrid-based NFC/BNNT to investigate the effect of incorporation of BNNT on k values of NFC-based materials. Three molecular models with similar combined weight content of NFCs and BNNTs are constructed to achieve this. Each NFC chain and BNNT in the three models have lengths of approximately 38 nm and 40 nm, respectively, due to the diminished increase of the rate of k for those lengths, as previously demonstrated in figures 1 and 2. The models are labeled as '100% NFC', '0% NFC' and '50% NFC', where 'X' in 'X % NFC' denotes the weight content of NFC in the model. The '100% NFC' model consists of 14 aligned NFC molecular chains, with its end (top panel) and side (bottom panel) views shown in figure 3(a). The '0% NFC' model comprises two aligned (10, 10) BNNTs, and their end (top panel) and side (bottom panel) views are displayed in figure 3(b). Lastly, the '50% NFC' model consists of the hybrid, where one middle BNNT is surrounded by seven NFC molecular chains, as demonstrated in figure 3(c) (end view—top panel; side view—bottom panel). The '100% NFC', '0%

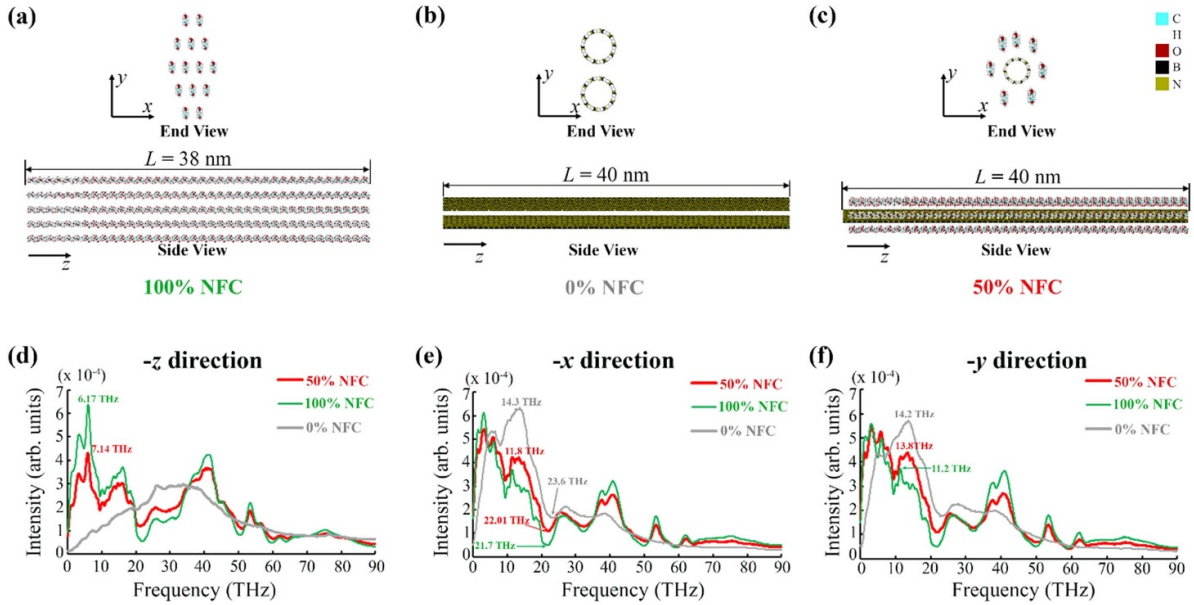

Figure 4. (a)–(c) Initial snapshots of the three models—(a) '100% NFC', (b) '0% NFC' and (c) '50% NFC', which are used to compute the DOS; (d)–(f) DOS plots along the (d) heat transfer direction ($-z$) and the out-of-plane (e) $-x$ and (f) $-y$ directions for the models. Intensity (arbitrary units) is denoted along the vertical axis and frequency (THz) is plotted along the horizontal axis.

NFC,' and '50% NFC' models contain 22 358, 12 880, and 17 619 atoms, respectively. The temperature profiles, obtained from RNEMD simulations, for each of the '100% NFC', '0% NFC' and '50% NFC' models are shown in figures 3 (d)–(f), respectively. The lowest value of k is observed for pure NFCs ('100% NFC model') at 0.746 W mK^{-1} (figure 3(g)). It is noteworthy that k for a single NFC molecular chain was higher ∼1.66 W mK^{-1}, as discussed in figure 1(c). However, when NFC molecules with identical lengths form a bundle (figure 3(a)), k decreases due to the higher phonon scattering between the neighboring molecular chains and edges, which has been previously observed in cellulose [14] and other polymers [36]. The highest value (∼68.29 W mK^{-1} as in figure 3(g)) is obtained for the pure BNNT ('0% NFC' model). On introducing BNNT into the NFC structures, k increased from 0.746 W mK^{-1} ('0% NFC' model) to 24.38 W mK^{-1} ('50% NFC' model). It can thus be concluded that improving thermal transport in NFC-based materials is indeed possible, by taking advantage of the high individual thermal conductivity exhibited by BNNTs.

To elucidate the phonon modes responsible for the increase in k upon incorporating BNNT into NFC-based materials, the vibrational DOS is computed for three models: '100% NFC', '0% NFC' and '50% NFC' models. To achieve equilibration states, the initial distance between NFC and BNNT (figure 4(c)) is maintained at 6 Å. This choice ensures that each molecule is not immediately influenced by neighboring groups but gradually relaxes and naturally interacts with its neighbors before calculating k and DOS. The DOS spectra, calculated along perpendicular directions ($-x$, $-y$, $-z$), are depicted in figure 4(a) ('100% NFC'), figure 4(b) ('0% NFC') and figure 4(c) ('50% NFC'). Figure 4(d) shows the DOS spectra of the three models along the thermal transport direction ($-z$), while the spectra across the out-of-plane directions are shown in figure 4(e) ($-x$ direction) and figure 4(f) ($-y$ direction). Consistent color coding is employed for plot lines representing different models (green for '100% NFC,' gray for '0% NFC' and 'red' for '50% NFC'). On comparing the DOS plots along each direction, it is evident that pure BNNTs ('0% NFC' model) facilitate thermal transport through transverse, out-of-plane vibrational modes ($-x$ wise and $-y$ wise). This can be attributed to their low frequency (∼0–20 THz) phonon modes, which significantly influence k; these modes exhibit peaks at approximately 14.3 THz (figure 4(e)) along $-x$ and around 14.2 THz (figure 4(f)) along $-y$ directions, respectively. However, in the case of pure NFCs ('100% NFC' model), the thermal transport is governed by in-plane ($-z$ wise) vibrational modes, as evidenced by the low-frequency spectral peak at ∼6.17 THz (figure 4(d)). On incorporating BNNT into NFCs, the corresponding peak shift from 6.17 to 7.14 THz for the hybrid (inset, figure 4(d)). This shift towards high energy and frequency denotes higher phonon energy carrying capacity in the hybrid, ultimately bolstering their k value. When comparing the transverse directions of the three structures to assess the impact of incorporating BNNT, it is observed that the analogous low-frequency peaks exhibit a subdued intensity. The maximum intensity is observed for BNNTs, while the minimum intensity is observed for NFCs, with the hybrid peak intensity in between. For instance, upon examining figure 4(f), it can be noted that the low-frequency peak for NFC occurs at approximately 11.2 THz with an intensity of around 3.41 × 10^{-4} units. The hybrid exhibits a peak at a similar frequency (∼13.8 THz) with a relatively higher intensity of 4.29 × 10^{-4} units. In comparison, the BNNT peak at ∼14.2 THz demonstrates a maximum intensity of (∼5.62 × 10^{-4} units). The same phenomenon is also

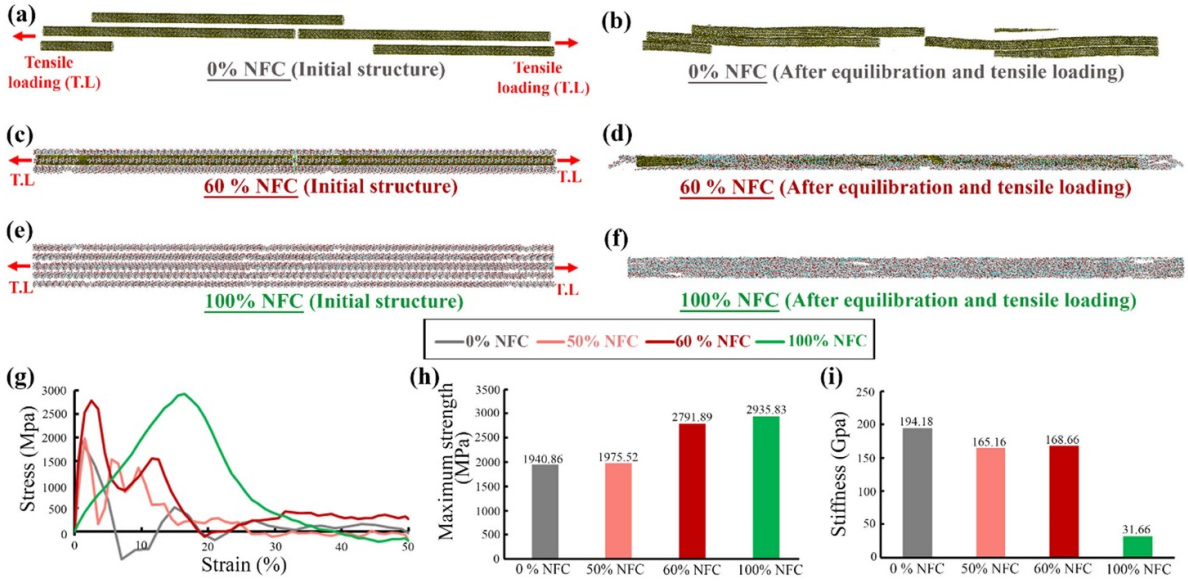

Figure 5. Comparison of mechanical properties with varying weight content of NFCs ('0% NFC', '50% NFC', '60% NFC' and '100% NFC'); (a)–(f) Simulation snapshots of three representative models ('0% NFC' in (a), (b); '60% NFC' in (c), (d) and '100% NFC' in (e), (f) before (a), (c), (e) and after (b), (d), (f) tensile deformation. Tensile loading directions shown by red arrows in (a), (c), and (e); (g) Plots reporting the engineering stress (MPa)-strain (%) values for the four models (gray for '0% NFC', light red for '50% NFC', red for '60% NFC' and green for '100% NFC'); (h)–(i) Comparison of (h) maximum strength (in MPa) and (i) stiffness (in GPa) for the four models as obtained from the stress-strain plots.

observed prominently in other lower frequency vibrational crests (∼20 THz) along both $-x$ (figure 4(e)) and $-y$ (figure 4(f)) directions. For pure NFCs, the spectral intensity is diminished due to the mobility of sliding NFC molecular chains along all degrees of freedom when heated, resulting in a higher state of disorder in the molecular domain. The introduction of crystalline BNNTs into NFCs leads to a reduction in this disorder. This explains why the corresponding spectral peak for the hybrid material is higher than that observed in pure NFCs. Furthermore, the peak intensity in BNNT is the highest due to their crystalline nature, which helps mitigate disorder compared to other materials. This, combined with the enhanced energy-carrying capacity of phonons, could potentially account for the increase in thermal conductivity while incorporating BNNTs into NFC structures.

The mechanical properties of structures with the same constituent fiber lengths (NFC ∼ 38 nm and BNNT ∼ 40 nm) as those used to investigate thermal conductivity previously are further examined. The objective is to assess the mechanical properties of the NFC/BNNT-based hybrid compared to pure NFC and BNNT structures. In this study, four similar models are constructed: '0% NFC' (pure BNNT), '50% NFC' (NFC:BNNT = 1:1 by weight), '60% NFC' (NFC:BNNT = 3:2 by weight), and '100% NFC' (pure NFC). The hybrid models are created with comparable weight contents as employed in experimental studies [23, 37–40]. The '0% NFC', '50% NFC', '60% NFC' and '100% NFC' models contain 25 760, 35 238, 48 014 and 44 716 atoms, respectively. The initial simulation snapshots of three representative models, '0% NFC', '60% NFC' and '100% NFC' are demonstrated in figures 5(a), (c) and (e), respectively. The initial structures are placed starting randomly in a linear fashion (along tensile loading direction as indicated by red arrows in figures 5(a), (c) and (e)). Periodic boundary conditions ensure each molecule emerging from one end of the simulation box to be mapped onto the opposite end. For the '0% NFC' model, there are four (10,10) BNNTs (figure 5(a)). The '50% NFC' and '60% NFC' (figure 5(b)) consist of 14 and 22 NFC molecular chains surrounded by two BNNTs. For the '100% NFC' model (figure 5(c)), there are 28 molecular chains of aligned NFCs. Before equilibration, the initial distance between each molecular chain and nanotubes is kept consistent at 6 Å (same as figure 4). Snapshots corresponding to tensile loading for the different models are presented in figures 5(b), (d) and (f) for 0% NFC, 60% NFC, and 100% NFC models, respectively. Consistent with previous findings [41], it is observed that the failure happens predominantly by inter-fiber sliding. The NFCs stick to the BNNTs in the hybrid due to strong interactions between them and are more mobile (protruding across the ends, as in figure 5(d)) than the BNNTs during the tensile deformation.

Figure 5(g) plots an engineering stress-strain graph to confirm that NFCs play a dominant role in increasing the mechanical strength of the NFC/BNNT composite. Pure BNNTs exhibit the lowest maximum strength ('0% NFC' model; gray lines in figures 5(g) and (h)) at ∼1940.9 MPa. On introducing NFC to 50% wt. content (total wt. remaining same as the '0% NFC' model), the maximum strength increased to ∼1975.5 MPa ('50% NFC' model shown by 'light red' lines in figures 5(g) and (h)). On further increasing the wt. content of NFCs to ∼60%, the maximum strength increased to ∼2791.9 MPa ('60% NFC' model displayed by 'dark red'

lines in figures 5(g) and (h)). Notably, the structure with pure NFCs ('green' lines in figures 5(g) and (h)) demonstrated the highest maximum tensile strength at ∼2935.8 MPa, which is comparable to recent modeling-based investigations [42]. The increase of maximum tensile strength due to the presence of NFCs in the composite is mainly because under tensile deformation, inter-fiber sliding occurs, and the NFCs undergo repetitive events of intermolecular hydrogen bonds breaking and reforming. This delays the tensile failure in the resulting material. In contrast, structures based on pure BNNTs lack such morphology-dependent events and have a much faster failure rate and, consequently, lower tensile strength. This is further evident from the fact that in pure NFC (green lines in figure 5(g)), the maximum strength is reached at a strain of ∼16%, in comparison to ∼1% strain for '0% NFC' structure and at ∼1.5% strain for the hybrid composites ('50% NFC' and '60% NFC' models). However, the stiffness (figure 5(i)) of pure NFCs ('100% NFC' model) is calculated to be ∼31.66 GPa (comparable with experimental results ∼23.9 GPa [43]), which was much lower than that of pure BNNTs (∼194.18 GPa as obtained from '0% NFC' model). Compared to pure NFC structures, the hybrids' stiffness was much higher at 165.16 GPa and 168.66 GPa for the '50% NFC' and '60% NFC' structures, respectively. This indicates that BNNTs, which individually have higher stiffness ranging from GPa to TPa (∼0.5–1.5 TPa [44–46]), impart elevated stiffness to the hybrid. The NFCs adhere to the BNNTs in the hybrid materials, thereby increasing the stiffness of the composite compared to pure NFC-based structures. Hence, BNNTs and NFCs play a mutually beneficial role in improving mechanical properties. While BNNT contributes to increased stiffness, NFCs predominantly upgrade the strength, resulting in a high-strength and high-stiffness material. Therefore, the combination of NFC/BNNT is an ideal choice for applications requiring superior mechanical properties and enhanced thermal conductivity due to their synergistic effect in improving thermo-mechanical properties.

4. Conclusions

In summary, the fundamental understanding behind the role of BNNTs incorporated into nanocellulose-based materials to elevate thermal conductivity is delineated. The thermal conductivity of pure nanocellulose structures investigated using reverse MD simulations was found to be relatively low at ∼0.746 W mK^{-1}. On introducing BNNTs by 50% wt. content in the nanocellulose/boron nitride composite, the thermal conductivity increased to ∼24.38 W mK^{-1}. Furthermore, the composite's phonon vibrational DOS was compared with pure BNNT and pure cellulose structures having equivalent total weight to identify the primary phonon vibrational modes driving the thermal transport in the nanocellulose-based hybrid. The individual roles of NFCs and boron–nitride nanotubes in increasing mechanical properties (e.g. tensile strength, stiffness) of the derived hybrid material are also discussed. The maximum tensile strength of the pure BNNTs structure (0% wt. content of nanocellulose) was observed to be lowest at ∼1940.9 MPa. But the tensile strength increased to ∼1975.5 MPa and ∼2791.9 MPa when the nanocellulose wt. content in the composite increased to 50% and 60%, respectively, emphasizing the vital role nanocellulose played in improving the hybrid material's mechanical strength. The stiffness of the pure nanocellulose material, however, was much lower at ∼31.66 GPa when compared with the pure boron nitride nanotube (∼194.18 GPa) structure. But for composites having 50% and 60% wt. content of nanocellulose, the stiffness was found to be 165.16 GPa and 168.66 GPa, respectively. This insinuates that while nanocellulose plays a crucial role in increasing the mechanical strength, BNNTs impart higher stiffness to the composite. This research calls for further studies to fabricate cellulose and BNNTs-based composites and obtain functional materials having increased thermal conductivity and superior mechanics. Such novel hybrids might be utilized in numerous future applications [47–55] pertaining to separators, flexible electronics, sensing, and thermal management.

Data availability statement

All data that support the findings of this study are included within the article (and any supplementary files).

Acknowledgments

The authors acknowledge the University of Maryland supercomputing resources (http://hpcc.umd.edu) made available for conducting the research reported in this paper. T L acknowledges the support of the US National Science Foundation (Grants Nos.1362256, 1936452). Z P acknowledges the support from the National Natural Science Foundation of China (NSFC) (Grant No. 12302143).

Conflict of interest

The authors declare that they have no conflict of interest.

ORCID iDs

Upamanyu Ray https://orcid.org/0000-0002-5290-7486
Teng Li https://orcid.org/0000-0001-6252-561X

References

[1] Ray U, Zhu S, Pang Z and Li T 2021 *Adv. Mater.* **33** 2002504
[2] Ray U, Zhu S, Pang Z and Li T 2023 Nanocellulose-based materials with superior mechanical performance *Emerging Nanotechnologies in Nanocellulose. NanoScience and Technology* ed L Hu, F Jiang and C Chen (Springer) (https://doi.org/10.1007/978-3-031-14043-3_5)
[3] Li K *et al* 2021 *ACS Nano* **15** 3646
[4] Lamm M E *et al* 2021 *Adv. Mater.* **33** 2005538
[5] Li T *et al* 2021 *Nature* **590** 47
[6] Peterson A *et al* 2021 *Macromolecules* **54** 3507
[7] Zhu H, Zhu S, Jia Z, Parvinian S, Li Y, Vaaland O, Hu L and Li T 2015 *Proc. Natl Acad. Sci.* **112** 8971

[8] Jarvis M C 2023 *Cellulose* **30** 667
[9] Ray U, Pang Z and Li T 2022 *J. Appl. Phys.* **132** 210703
[10] Uetani K and Hatori K 2017 *Sci. Technol. Adv. Mater.* **18** 877
[11] Diaz J A, Ye Z, Wu X, Moore A L, Moon R J, Martini A, Boday D J and Youngblood J P 2014 *Biomacromolecules* **15** 4096
[12] Zeng X, Sun J, Yao Y, Sun R, Bin Xu J and Wong C P 2017 *ACS Nano* **11** 5167
[13] Yang W and Kim J 2022 *Ceram. Int.* **48** 25284
[14] Dong R Y, Dong Y, Li Q and Wan C 2020 *Int. J. Heat Mass Transfer* **148** 119155
[15] Diaz J A, Wu X, Martini A, Youngblood J P and Moon R J 2013 *Biomacromolecules* **14** 2900
[16] Zhi C, Bando Y, Tang C and Golberg D 2010 *Mater. Sci. Eng.* R **70** 92–111
[17] Golberg D, Bando Y, Tang C and Zni C 2007 *Adv. Mater.* **19** 2413
[18] Huang J, Guo Y, Fan Y and Liang Y 2020 *Mater. Res. Express* **7** 025025
[19] Wang L, Han D, Luo J, Li T, Lin Z and Yao Y 2018 *J. Phys. Chem.* C **122** 1867
[20] Simonsen Ginestra C J *et al* 2022 *Nat. Commun.* **13** 3136
[21] Tang C, Bando Y, Liu C, Fan S, Zhang J, Ding X and Golberg D 2006 *J. Phys. Chem.* B **110** 10354
[22] Zhi C, Bando Y, Terao T, Tang C, Kuwahara H and Golberg D 2009 *Adv. Funct. Mater.* **19** 1857
[23] Huang X, Zhi C, Jiang P, Golberg D, Bando Y and Tanaka T 2013 *Adv. Funct. Mater.* **23** 1824
[24] Terao T, Zhi C, Bando Y, Mitome M, Tang C and Golberg D 2010 *J. Phys. Chem.* C **114** 4340
[25] Khoury J F, Vitale J C, Larson T L and Ao G 2022 *Nanoscale Adv.* **4** 77
[26] Wang C, Jagirdar P, Naserifar S and Sahimi M 2016 *J. Phys. Chem.* B **120** 1273
[27] Zhu M, Li J, Chen J, Song H and Zhang H 2019 *Comput. Mater. Sci.* **164** 108
[28] Fu C *et al* 2018 *Compos. Sci. Technol.* **165** 322
[29] Plimpton S 1995 *J. Comput. Phys.* **117** 1–19
[30] Thompson A P *et al* 2022 *Comput. Phys. Commun.* **271** 108171
[31] Chenoweth K, Van Duin A C T and Goddard W A 2008 *J. Phys. Chem.* A **112** 1040
[32] Aktulga H M, Pandit S A, Van Duin A C T and Grama A Y 2012 Reactive molecular dynamics: numerical methods and algorithmic techniques *SIAM J. Sci. Comput.* **34** C1–C23
[33] Ambekar R S, Deshmukh A, Suárez-Villagrán M Y, Das R, Pal V, Dey S, Miller J H, Machado L D, Kumbhakar P and Tiwary C S 2020 *ACS Appl. Mater. Interfaces* **12** 45274
[34] Müller-plathe F 1997 *J. Chem. Phys.* **106** 6082
[35] Uetani K, Okada T and Oyama H T 2015 *Biomacromolecules* **16** 2220–7
[36] Luo T, Esfarjani K, Shiomi J, Henry A and Chen G 2011 *J. Appl. Phys.* **109** 074321
[37] Sato K, Horibe H, Shirai T, Hotta Y, Nakano H, Nagai H, Mitsuishi K and Watari K 2010 *J. Mater. Chem.* **20** 2749
[38] Zhi C Y, Bando Y, Wang W L, Tang C C, Kuwahara H and Golberg D 2008 *Nanomater. J.* **2008** 642036
[39] Zhu H, Li Y, Fang Z, Xu J, Cao F, Wan J, Preston C, Yang B and Hu L 2014 *ACS Nano* **8** 3606
[40] Kemaloglu S, Ozkoc G and Aytac A 2010 *Polym. Polym. Compos.* **31** 1398
[41] Ray U, Pang Z and Li T 2021 *Cellulose* **28** 3359
[42] Zhang X and Zhu S 2023 *Extrem. Mech. Lett.* **62** 102035
[43] Kafy A, Kim H C, Zhai L, Kim J W, Van Hai L, Kang T J and Kim J 2017 *Sci. Rep.* **7** 17683
[44] Chen X, Zhang L, Park C, Fay C C, Wang X and Ke C 2015 *Appl. Phys. Lett.* **107** 253105
[45] Ghassemi H M, Lee C H, Yap Y K and Yassar R S 2010 *J. Appl. Phys.* **108** 024314
[46] Li T, Tang Z, Huang Z and Yu J 2017 *Physica* E **85** 137
[47] Sathwane M, Chhajed M, Verma C, Gaikwad K K and Maji P K 2023 *Polym. Compos.* **44** 492
[48] Lu Y, Zhao R, Wang L and Diam S E 2023 *Relat. Mater.* **136** 109978
[49] Lee C H, Bhandari S, Tiwari B, Yapici N, Zhang D and Yap Y K 2016 *Molecules* **21** 922
[50] Yu L, Gao T, Mi R, Huang J, Kong W, Liu D, Liang Z, Ye D and Chen C 2023 *Nano Res.* **16** 7609–17
[51] Trache D, Tarchoun A F, Derradji M, Hamidon T S, Masruchin N, Brosse N and Hussin M H 2020 Nanocellulose: from fundamentals to advanced applications *Front. Chem.* **8** 392
[52] Chen C *et al* 2023 *Adv. Funct. Mater.* **33** 2370002
[53] Nepal D *et al* 2023 *Nat. Mater.* **22** 18–35
[54] Zhou M, Wang J, Zhao Y, Wang G, Gu W and Ji G 2021 *Carbon* **183** 515
[55] Thomas B, Raj M C, Athira B K, Rubiyah H M, Joy J, Moores A, Drisko G L and Sanchez C 2018 *Chem. Rev.* **118** 11575